The effect of substrate clamping on the paraelectric to antiferroelectric phase transition in Nd-doped BiFeO$_3$ thin films

H.R. Zhang [a], K. Kalantari [a], D.M. Marincel [b,1], S. Trolier-McKinstry [b], I. MacLaren [c], Q.M. Ramasse [d], W.M. Rainforth [a], I.M. Reaney [a,*]

[a] Department of Materials Science & Engineering, University of Sheffield, Sheffield S1 3JD, UK
[b] Department of Materials Science and Engineering, Materials Research Institute, The Pennsylvania State University, University Park, PA 16802, USA
[c] School of Physics and Astronomy, University of Glasgow, Glasgow G12 8QQ, UK
[d] SuperSTEM Laboratory, SciTech Daresbury Campus, Daresbury WA4 4AD, UK

ARTICLE INFO

ABSTRACT

Thin films were deposited on Pt/Ti/SiO$_2$/Si substrates using pulsed laser deposition from a target with a composition (Bi$_{0.825}$Nd$_{0.175}$Fe$_{0.97}$Ti$_{0.03}$O$_3$) with 5 mol% excess Bi$_2$O$_3$ within the antiferroelectric (AFE) region of the NdFeO$_3$-BiFeO$_3$ phase diagram. However, Raman spectroscopy and transmission electron microscopy (TEM) revealed that films consisted of a mosaic microstructure in which (AFE), ferroelectric (FE) and paraelectric (PE) phases coexisted. Variation in the spatial distribution of Nd is typically greater in bulk ceramics than in thin films and therefore, the absence of single phase AFE cannot be attributed to local changes in composition. Instead, it is proposed that clamping due to mismatch in thermal expansion coefficient with the substrate suppresses the large volume change associated with the PE-FE and PE-AFE transition in bulk and its absence in the thin film prevents an avalanche-like transition throughout grains, which in bulk sustains single phase AFE, irrespective of local deviations in the Nd concentration.

© 2016 The Authors. Published by Elsevier B.V. This is an open access article under the CC BY license (http://creativecommons.org/licenses/by/4.0/).

1. Introduction

BiFeO$_3$ (BFO) has recently attracted enormous interest due to the co-existence of ferroelectricity and antiferromagnetism above room temperature [1,2]. BiFeO$_3$ has the perovskite structure with a rhombohedral distortion along the [111] direction and a Neel temperature at ~370 °C [3]. Although BiFeO$_3$ is an environmentally friendly compound upon which to base functional materials and devices, it suffers from high leakage current, large coercive fields and low electromechanical coefficients [4]. However, A and B site doping of BiFeO$_3$ has been shown to improve leakage resistance [5,6] and the electromechanical response [4]. Typically, isovalent A-site doping is carried out using various rare-earth (RE) cations. Not only do they control the leakage behaviour, but due to the lower polarizability of RE ions in comparison with Bi, the phase transition temperature (T$_C$) decreases [5,6]. Further control over leakage current can be achieved by donor doping the B-site with higher valence species such as Ti^{4+} and Nb^{5+} which even at low concentrations (1–3 mol%) significantly decrease the conductivity of bulk ceramics and increase the activation energy for conduction [7,8]. However, donor doping Bi$_{1-x}$RE$_x$FeO$_3$ without ionic compensation on the A-site through V$_{RE}$ has been shown to lead to the ex-solution of the RE oxide, resulting in the formation of coherent precipitates of RE$_2$O$_3$ embedded in the perovskite matrix [7].

At high enough concentrations, RE substitution results in a phase transition from the rhombohedral ferroelectric (FE) into a PbZrO$_3$ (PZ)-like antiferroelectric (AFE) structure [5,6]. Although this has been extensively demonstrated in bulk ceramics (Nd doped compositions are considered to have an AFE phase field from 14 to 22 mol% Nd), there have been no reports of single phase AFE thin films for any RE containing system [9,10]. Most attention in the scientific literature has focussed on Sm-doped compositions which even as bulk ceramics with multiple grinding and heating have only a narrow PZ-like phase field (1 mol% wide) at 14 mol% Sm above which a paraelectric (PE) phase is observed [10]. Thin films have therefore consistently been reported to be multi-phase with compositions being either mixtures of AFE/FE or AFE/PE [9], due to the narrow compositional phase field.

Despite the absence of single-phase thin films, compositions around the AFE/FE phase boundary have been reported to exhibit a peak in piezoelectric activity and thus have received attention as potential PbO-free replacements for Pb(Zr,Ti)O$_3$ [4]. The purpose of this contribution is to explore the possibility that single-phase AFE compositions can be fabricated as thin films and thus determine whether AFE to FE switching is feasible in a manner reported for PbO-based compositions. To this end, the bulk ceramic composition, Bi$_{0.825}$Nd$_{0.175}$Fe$_{0.97}$Ti$_{0.03}$O$_3$ (BNFO) with 5 mol% excess Bi$_2$O$_3$, was fabricated as a target for pulsed laser

* Corresponding author.
E-mail address: I.M.Reaney@sheffield.ac.uk (I.M. Reaney).
[1] Department of Chemical and Biomolecular Engineering, Rice University, Houston, TX 77005, USA.

deposition (PLD) of films on Pt/Ti/SiO$_2$/Si substrates. The composition was chosen since it lies in the centre of the AFE phase field, as reported by Levin and co-workers [11] and thus provides the optimum composition assess whether it is feasible to deposit single phase AFE BiFeO$_3$ based films. Note that Ti doping on the B-site is used to control conductivity in the BNFO, as described by Kalantari et al. [7,8]

2. Experimental procedure

BNFO films were deposited on Pt/Ti/SiO$_2$/Si substrates using a 248 nm KrF excimer laser from a target with composition, Bi$_{0.825}$Nd$_{0.175}$Fe$_{0.97}$Ti$_{0.03}$O$_3$ (BNFO) with 5 mol% excess Bi$_2$O$_3$. The target was fabricated using a conventional solid state route (calcined 3 h at 960 °C and sintered 3 h at 990 °C) to >95% theoretical density with all peaks attributed to a PZ-like structure (*Pbam*). Prior to deposition, substrates were ultrasonically cleaned sequentially in acetone, ethanol, and isopropanol. The BNFO films were deposited on substrates at either 625 °C or 650 °C, at a 75 mTorr chamber pressure, using a laser energy density of 2.5 J·cm^{-2} and a repetition rate of 10 Hz. A 10% O$_3$/90% O$_2$ ambient was used for all the depositions. To reduce non-uniform erosion as well as droplet formation, targets were rotated during the ablation process. Immediately after deposition, the samples were cooled to 400 °C under the same pressure of O$_3$/O$_2$ to minimize the possibility of evaporation of volatile species.

Secondary electron images were obtained using an FEI Inspect F scanning electron microscope (SEM) operating at 20 keV. Samples were mounted on Al stubs using Ag paste and gold sputter coated to prevent charging. X-ray diffraction analysis was carried out using a Philips Analytical X-ray diffractometer (PANalytical XPert Pro MPD; Philips, Westborough, MA) using Cu Kα radiation to assess the film crystal structure and orientation. Cross sections of the films for TEM were prepared using a dual beam FIB/SEM FEI Quanta 3D 200. Specimens were thinned at a low angle and low voltage toward the end of the process to reduce ion-beam damage. Conventional electron microscopy was performed using a JEOL2010F microscope operating at 200 keV. High resolution transmission electron microscopy (HRTEM) analysis was performed on a double aberration-corrected microscope JEM-Z3100F-R005 STEM/TEM operated at 300 keV in TEM mode with a positive spherical aberration (C$_s$) coefficient ~ 3 μm and slightly negative/positive defocus. Atomic resolution high angle annular dark field (HAADF) scanning transmission electron microscopy (STEM) and electron energy loss spectroscopy (EELS) spectrum-imaging analyses were performed on a Nion UltraSTEM microscope operated at 100 keV. The microscope optical parameters were adjusted to create a ~ 0.9 Å probe, with a convergence semi-angle of 31 mrad. The HAADF detector semi-angular collection range was 85–190 mrad, while EEL spectra were collected using a Gatan Enfina spectrometer through a 36 mrad (semi-angle) entrance aperture. Chemical maps were generated from spectrum images (whereby the electron probe is scanned across a defined area of the sample, acquiring both image and energy loss signals at each pixel) by integrating the EELS intensity over a suitable energy
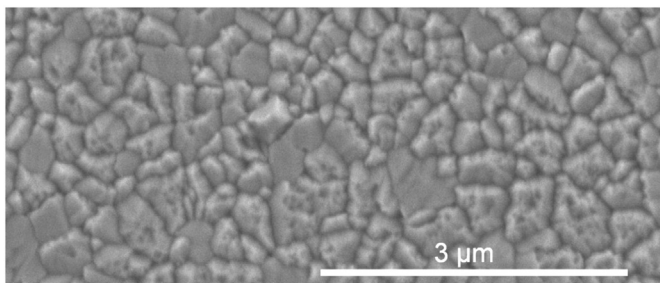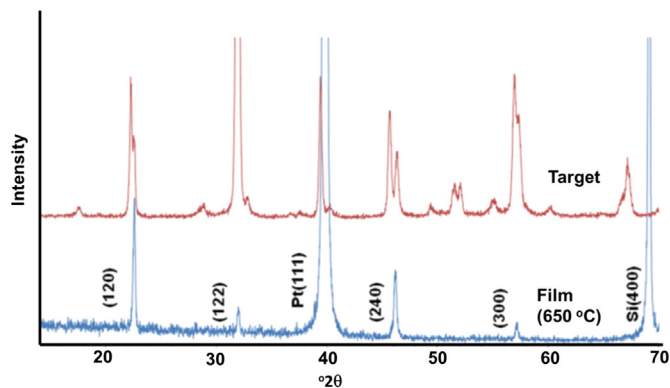

Fig. 2. XRD patterns of BNFO bulk ceramic target and thin film deposited at a substrate temperature of 650 °C.

window (typically 30–50 eV) for the relevant ionisation edges, after subtraction of the decaying background using a power-law fit. To increase the signal-to-noise, the HAADF images were obtained by rigid registration of stacks (of up to 20) individual images of the same area acquired in rapid succession using short pixel dwell times.

Unpolarised Raman spectra were excited with the 514.5 nm line of an Ar laser and recorded in back scattering geometry using a Renishaw InVia micro-Raman spectrometer. For this purpose, a laser power of 4 mW was focused on a ~ 2 um spot. The spectral resolution was ~1 cm^{-1}. The spectra were evaluated in a comparative manner.

3. Results and discussion

3.1. Scanning electron microscopy

Fig. 1 shows a secondary electron image of the surface of a thin film deposited at a substrate temperature of 625 °C. Similar images were obtained for 650 °C deposition. The morphology and grain size (<0.2 μm) was the same over the entire film surface with no secondary phases apparent in backscattered images (not shown here).

3.2. X-ray diffraction

The XRD traces of thin films deposited at 625 °C and 650 °C are similar and may be indexed according to a fundamental perovskite lattice, with a preferred pseudocubic (001) orientation. Fig. 2 shows a trace of a film deposited at 650 °C, together with that of the bulk target which has the PZ-like structure, first described by Karimi et al. [5,6]. The
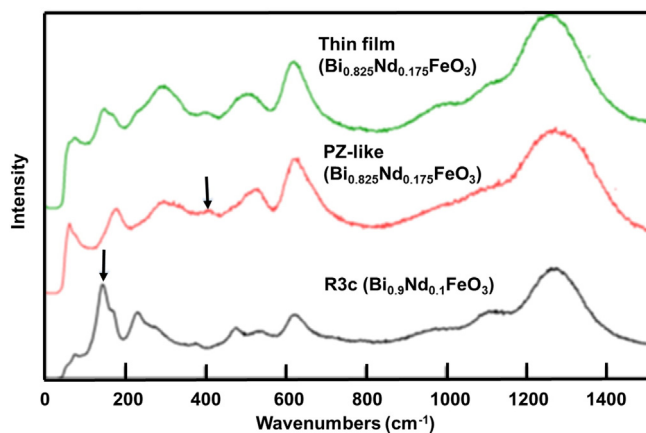

Fig. 1. Scanning electron micrograph of the surface of a BNFO film deposited at a substrate temperature of 625 °C.

Fig. 3. Raman spectra of a BNFO thin film and bulk ceramics which have PZ-like *Pbam* symmetry (BNFO: 17.5% Nd) and *R3c* symmetry (BNFO: 10% Nd).

unique reflections associated with the PZ-like phase at, e.g. ~18° and 28° are absent for the thin film, moreover the characteristic splitting of the peaks which also denotes the PZ-like cell is not observed. The absence, however, of conclusive weak reflections and peak splitting from thin films of distorted perovskites is not unusual and is normally attributed to a combination of preferred orientation, substrate clamping effects
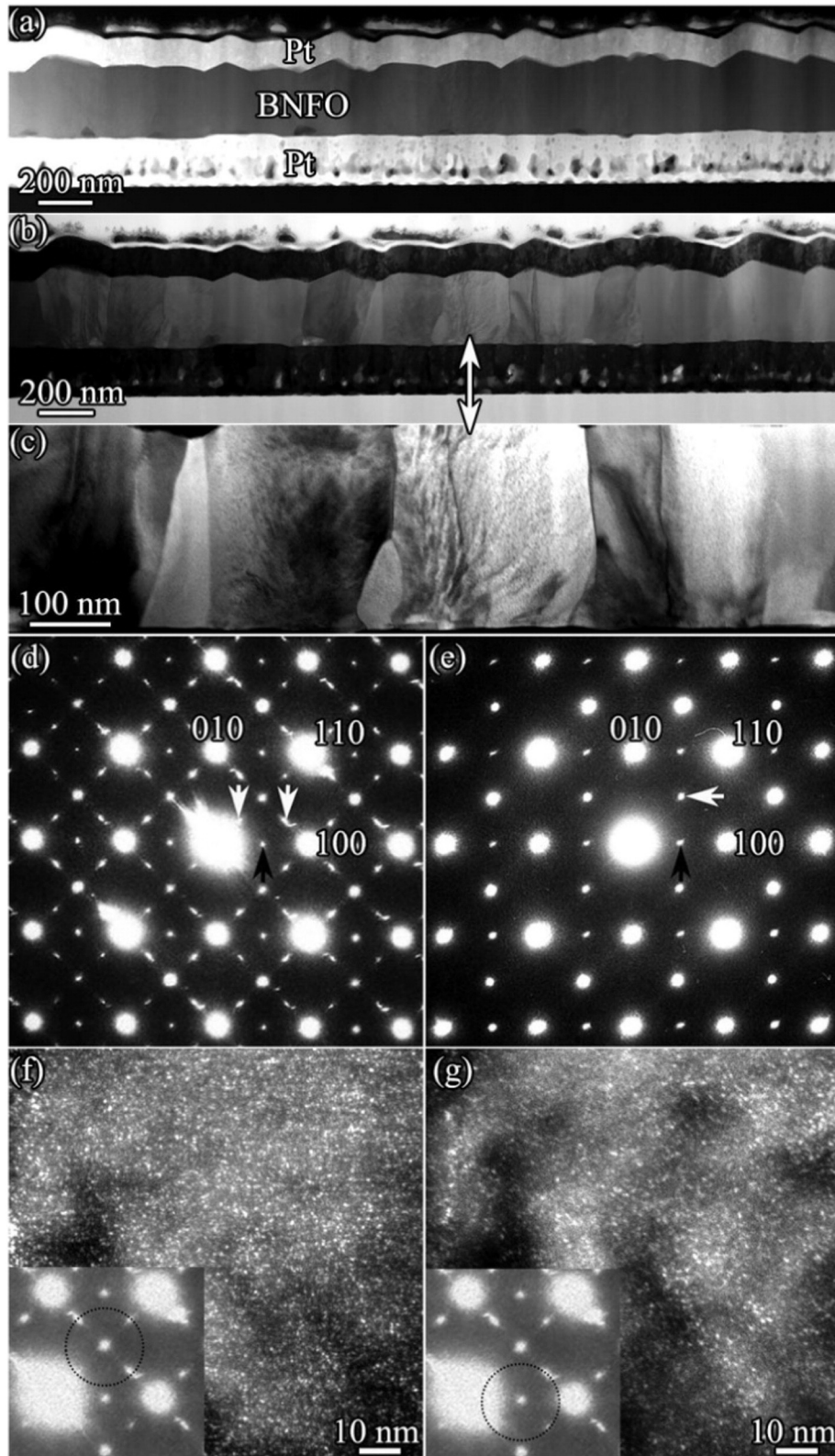

Fig. 4. (a) HAADF-STEM image and (b) corresponding bright field STEM image showing the BNFO film grown on Pt substrate and, (c) local enlarged image showing the strain-constrast in the grain. (d) and (e) selected area electron diffraction patterns taken from the same grain along the pseudo-cubic $[001]_c$ zone-axis in different areas. The white arrows showing the ¼{ooe} superlattice reflections from two 90° antiferroelectric variants (d), and ½{ooe} superlattice reflections from paraelectric variants (e). The black arrows showing the ½{oee} superlattice reflections from antiferroelectric or paraelectric variants. (f) and (g) were imaged with the smallest objective aperture and selecting the reflections of ½(110) + ¼(110), and ½(100) plus part of the ¼{110} reflections, as illustrated by the black dotted circles in the insets, respectively.

and weak intensity from a thin layer (225 nm). It is important therefore to ascertain a better understanding of the structure of the film, specifically whether the film has the ferroelectric, FE (*R3c*), an antiferroelectric PZ-like, AFE (*Pbam*) or paraelectric, PE (*Pnma*) distortion. Karimi et al. [6] reported that these symmetries may be readily distinguished using Raman spectroscopy and illustrated the key modes and bands associated with each phase.

3.3. Raman spectroscopy

Fig. 3 shows a set of room temperature Raman spectra of a thin film and two bulk ceramics. A Raman spectrum from a thin film deposited at 625 °C is compared with the bulk spectra from PZ-like and ferroelectric *R3c* structures, derived from $Bi_{0.825}Nd_{0.175}Fe_{0.97}Ti_{0.03}O_3$ and $Bi_{0.9}Nd_{0.1}Fe_{0.97}Ti_{0.03}O_3$ bulk samples, respectively [6]. Many film modes correspond to the AFE PZ-like structure but some are best described as arising from the ferroelectric *R3c* structure. For example, the thin film mode at 400 cm^{-1} is present in the PZ-like bulk spectrum while the sharper mode at 150 cm^{-1} exists only in the *R3c* spectrum. It is concluded therefore that thin films deposited at 625 °C (and 650 °C) contain PZ-like as well as *R3c* structures. TEM analysis is however, required to assess whether *R3c* and the PZ-like AFE are the only phases present and to determine the spatial distribution of the phase assemblage.

3.4. Transmission electron microscopy

Fig. 4(a) and (b) show a typical cross-section HAADF-STEM image and a bright-field STEM image of the BNFO film between the Pt electrodes. No second phases were detected. Fig. 4(c) shows a local enlarged image of 4(b). The arrowed grain shows strain contrast, typical of planar defects, such as domain or small angle boundaries. Fig. 4(d) and (e) show two selected area electron diffraction patterns (SAEDPs) taken from the same grain along the pseudocubic [001]$_c$ zone-axis in different areas. The white arrows in Fig. 4(d) show two sets of ¼{ooe} (where o = odd and e = even) superlattice reflections arising from 90° AFE variants (*Pbam*, $\sqrt{2}a \times 2\sqrt{2}a \times 2a$).[6] In contrast to the pure AFE phase exhibited by ceramic samples of this chemical composition [5,6], the PE phase (*Pnma*: $\sqrt{2}a \times \sqrt{2}a \times 2a$) was also detected in the thin film, as evidenced by the well-defined ½{ooe} superlattice reflection shown by the white arrow in Fig. 4(e). The ½{oee} superlattice reflections shown by the black arrows in both patterns are from other variants of either the AFE or PE structure. Diffraction-contrast imaging analysis was
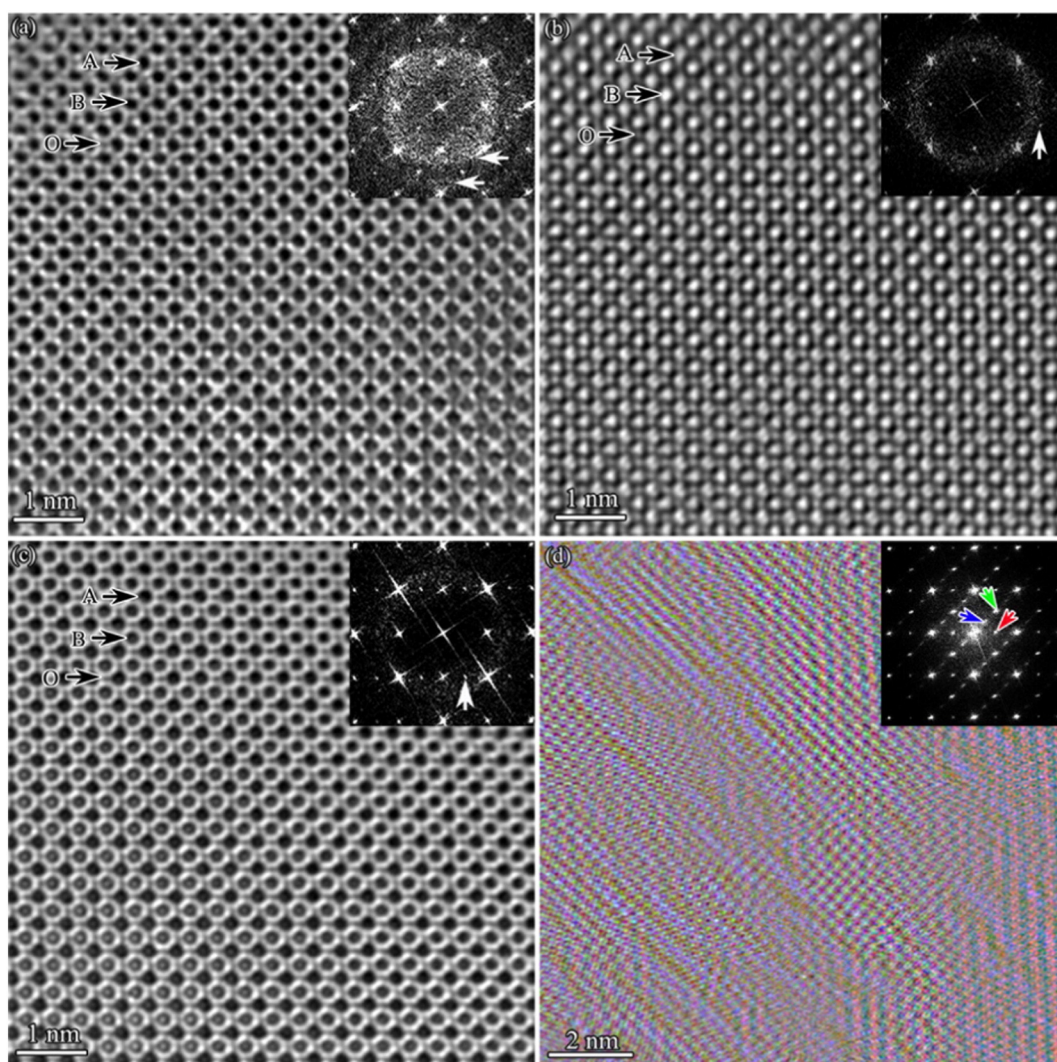

Fig. 5. HRTEM images taken from single grain along the pseudo-cubic [001]$_c$ zone-axis and the corresponding FT images showing (a) AFE domain, (b) PE domain, (c) AFE or PE domain, (d) RGB HRTEM image reconstructed from three images obtained by filtering the raw [001]$_c$ image using ½{100} reflections (red), ½{110} reflections (green) and ¼{110} reflections (blue) illustrated in the FT image (inset), respectively, showing an intergrowth of the AFE/PE nanodomains in local area. (For interpretation of the references to colour in this figure legend, the reader is referred to the web version of this article.)
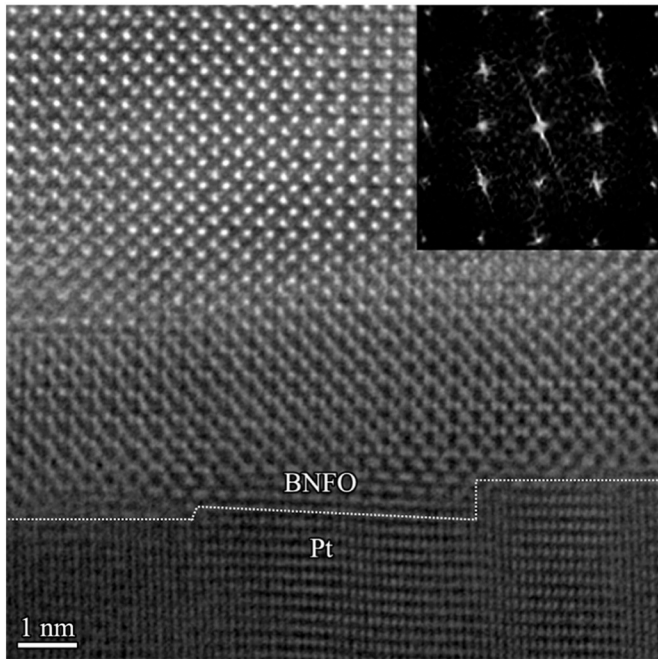
Fig. 6. HRTEM image of the interface region of BNFO film and Pt substrate, no superlattice reflections in the FT image of BNFO film along pseudo-cubic [001]$_c$ zone-axis (inset), suggesting a ferroelectric $R3c$ structure in local area.

performed to understand the distribution of the variants. Fig. 4(f) and (g) were imaged using the smallest objective aperture to select the superlattice reflections ½{ooe} + ¼{ooe}, and ½{ooe} plus part of a ¼{ooe} reflections as illustrated by the black dotted circle in the insets, respectively. The uniform distribution of the bright dots of ~2 nm in size in the diffraction-contrast may be interpreted as an intergrowth of nanosized AFE and PE domains. We note that some of bright contrast may arise from Nd-rich nanorods, observed in small quantities in thin films but abundant in bulk, as described by Kalantari and co-workers [7]. It is notable that the size of the domains is well below the crystallite size. However, due to the overlap of the nanosized domains, SAEDPs and

diffraction-contrast imaging analyses cannot exclude the existence of a FE phase ($R3c$: $\sqrt{2}a \times \sqrt{2}a \times 2\sqrt{3}a$) which has no superlattice reflections along pseudocubic [001]$_c$ zone-axes.

Aberration-corrected HRTEM, atomic resolution HAADF-STEM and EELS spectrum-imaging analyses were further performed to study the BNFO film. Fig. 5 shows the HRTEM images, with the corresponding Fourier Transforms (FT) (inset), taken from local areas of a single grain. In the thin area of the specimen edge, the atomic positions corresponding to the A-site, B-site and O-site can be identified, as shown in Fig. 5(a)–(c). The local AFE/PE domain structures were determined from the FT image with the characteristic ¼{ooe} reflections for $Pbam$ structure and ½{ooe} reflections for $Pnma$ structure, as shown in the inset of Fig. 5(a) and (b). When the domain is orientated with the ½{oee} reflections visible, as shown in Fig. 5(c), the AFE/PE domain cannot be differentiated easily. Fig. 5(d) shows a composite HRTEM image reconstructed from three images representing the AFE/PE domains (red), PE domains (green) and AFE domains (blue), respectively. The FT image (inset) of the raw image shows clearly that the superlattice reflections from AFE and PE co-exist within a single grain as intergrown variants. No well-defined boundary between the variants can be determined in the composite HRTEM image. The existence of intergrowths of different phases is consistent with the diffraction-contrast image analysis. Detailed HRTEM analysis was also performed in the interface region of the BNFO film and Pt substrate. As shown in the inset of Fig. 6, there are no superlattice reflections in the FT image of the pseudocubic [001]$_c$ BNFO film, suggesting that some local regions at the film/electrode interface that the phase have the ferroelectric $R3c$ structure, although other non-cell doubled ferroelectric phases are not excluded.

To better understand the crystal chemistry and defect chemistry of the BNFO film, atomic resolution HAADF-STEM and EELS spectrum-imaging analyses were carried out on a Nion UltraSTEM microscope operated at 100 keV. Fig. 7(a) shows a HAADF image taken along the pseudo-cubic [012]$_c$ zone-axis. The atomic image shows two intergrown variants which have different amplitudes of off-center displacement of the bright A-site atomic columns, as shown by the white dash-dot frames (Variant 1 and Variant 2). However, FT images of the two variants have a common ½⟨021⟩ superlattice reflection, as shown by the white arrow in Fig. 7(b). Detailed analysis on the diffraction patterns and atomic projections of all the variants of the equivalent pseudo-cubic ⟨012⟩$_c$ zone-axes reveals that these two variants belong to PE and AFE
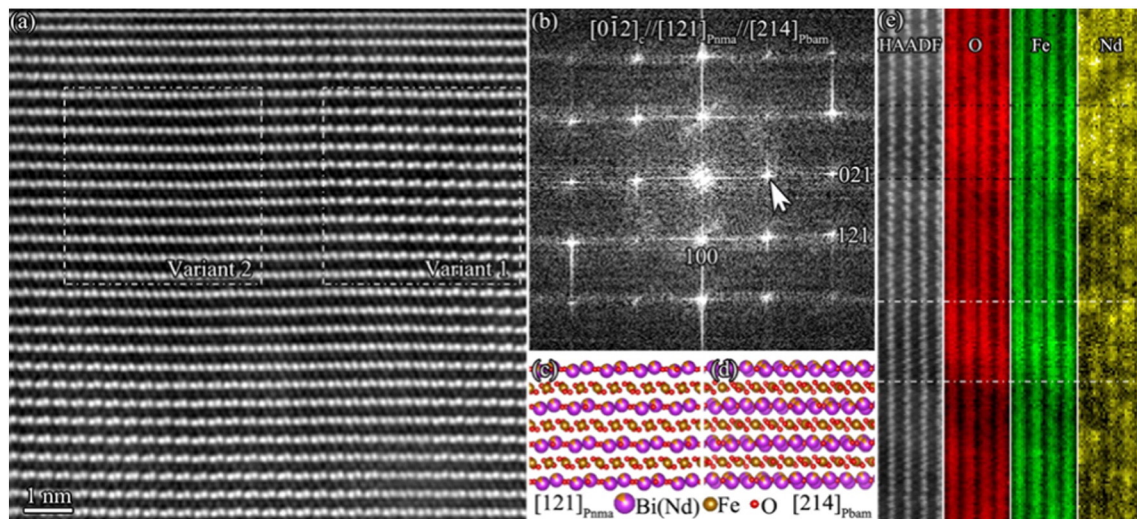

Fig. 7. (a) Atomic resolution HAADF-STEM image taken along pseudo-cubic [012]$_c$ zone-axis showing intergrowth of the variants. The FT images of Variant 1 and Variant 2 appear the same as in (b). White arrow showing the ½⟨021⟩ superlattice reflection shared by PE variant along [121]$_{Pnma}$ zone-axis and AFE variant along [214]$_{Pbam}$ zone-axis. (c) and (d) Atomic projection of [121]$_{Pnma}$ and [214]$_{Pbam}$, respectively. (e) Atomic resolution EELS spectrum-imaging analysis of the chemical maps of O, Fe, and Nd. The sampled region was partly contaminated by Pt top electrode during FIB milling. The black and white dash-dot lines define local clean areas with $Pnma$ and $Pbam$ structures, respectively. False colors were added in the maps for better visibility.

structures with projection along $[121]_{Pnma}$ and $[214]_{Pbam}$, as illustrated in Fig. 7(c) and (d), respectively.

Atomic resolution EELS spectrum-imaging analysis was performed to understand the elemental distribution in the variants. Fig. 7(e) shows the chemical maps of O, Fe, and Nd in a sampled region containing both the PE and AFE structures. The sampled region was partly contaminated by the Pt top electrode during FIB milling, which reduced the signal of O, Fe and Nd in the contaminated region due to a strong scattering of the incident electrons by Pt (also accounting for the slightly mottled contrast observed in the HAADF image in Fig. 7a). Two clean areas with stronger O and Fe signals are identified as *Pnma* and *Pbam* structures and are marked by black and white dash-dot lines, respectively. The chemical map shows a random distribution of Nd in the A-site, and a higher Nd content in the *Pnma* structure than in the *Pbam* structure which is qualitatively consistent with the previous study of crystal chemistry in the ceramic samples [5,6].

The phase assemblage of the films determined by XRD, Raman and TEM is complex, with PE, AFE and FE phases present. According to Levin et al. [11] and Kalantari et al. [8], the target composition lies firmly in the heart of the AFE phase field for bulk compositions. Bulk ceramics of these composition contain no evidence of residual FE or PE phase. Hence the multiphase, mosaic nature of the films is somewhat surprising. The fact that many of the phases were intergrown within a single grain suggests that macroscopic chemical partitioning is not primarily responsible for the complex phase assemblage. There are large volume changes associated with the PE-AFE and PE-FE transitions in bulk ceramics which are highly anisotropic (the b-axis distorts by ~2% in the AFE phase) [11]. This leads to large length changes observed by dilatometry and unusually sharp exotherms in differential scanning calorimetry [12]. We propose therefore, that the complex phase assemblage of thin film BNFO occurs in part through chemical heterogeneity but mainly through clamping due to the mismatch in thermal expansion between the Pt/Si substrate and the BNFO film. The grains form a mosaic microstructure to accommodate the stress state induced in the films, partially following local variations in composition. In the case of a pure ferroelectric film, strain accommodation due to thermal expansion mismatch often takes the form of orientation of the polarisation vector, but in BNFO (17.5% Nd), there is a further degree of freedom to accommodate strain due to the similar free energies of the PE, FE and AFE states. We note the Nd distribution in bulk ceramics is not homogeneous, yet these compositions are single phase AFE [5–9]. Bulk ceramics however, are composed of grains several microns in diameter with each grain clamped isotropically. This qualitative description of the ferroelastic boundary conditions is very different to those in thin films. We conclude therefore that the multiphase, intergrowth assemblage in thin films is principally due to the stress induced through thermal expansion mismatch between the substrate and film rather than solely chemical inhomogeneity.

4. Conclusions

Single phase polycrystalline $Bi_{0.825}Nd_{0.175}Fe_{0.97}Ti_{0.03}O_3$ thin films were fabricated by PLD on $Pt/Ti/SiO_2/Si$ substrates. SEM did not reveal any secondary phases and the grain morphology and size (0.2 μm) of the sample was consistent across the entire surface of the film. The target had the PZ-like, AFE structure but Raman spectroscopy and TEM studies revealed that films had intergrowths and regions of AFE, FE and PE phases. The absence of single phase AFE is attributed to clamping of the film due to thermal expansion mismatch with the Pt/Si substrate, which suppresses the avalanche-like transition from PE to AFE, responsible for the wide AFE phase field in bulk ceramics. Instead, the film stress state is accommodated by the formation of a mosaic of PE, FE and AFE phases.

References

[1] G. Catalan, J.F. Scott, Physics and applications of bismuth ferrite, Adv. Mater. 21 (2009) 2463.
[2] I. Sosnowska, T. Peterlin-Neumaier, E. Steichele, Spiral magnetic ordering in bismuth ferrite, J. Phys. C Solid State Phys. 15 (1982) 4835–4846.
[3] P. Fischer, M. Polomska, I. Sosnowska, M. Szymanski, Temperature dependence of the crystal and magnetic structures of $BiFeO_3$, J. Phys. C Solid State Phys. 13 (1980) 1931–1940.
[4] S. Fujino, M. Murakami, A. Varatharajan, S.-H. Lim, V. Nagarajan, C.J. Fennie, M. Wuttig, L. Salamanca-Riba, I. Takeuchi, Combinatorial discovery of a lead-free morphotropic phase boundary in a thin-film piezoelectric perovskite, Appl. Phys. Lett. 92 (2008), 202904.
[5] S. Karimi, I.M. Reaney, I. Levin, I. Sterianou, Nd-doped $BiFeO_3$ ceramics with antipolar order, Appl. Phys. Lett. 94 (2009) 112903.
[6] S. Karimi, I. Reaney, Y. Han, J. Pokorny, I. Sterianou, Crystal chemistry and domain structure of rare-earth doped $BiFeO_3$ ceramics, J. Mater. Sci. 44 (2009) 5102.
[7] I.M. Reaney, I. MacLaren, L. Wang, B. Schaffer, A. Craven, K. Kalantari, I. Sterianou, S. Miao, S. Karimi, D.C. Sinclair, Defect chemistry of Ti-doped antiferroelectric $Bi_{0.85}Nd_{0.15}FeO_3$, Appl. Phys. Lett. 100 (2012), 182902.
[8] K. Kalantari, I. Sterianou, S. Karimi, M.C. Ferrarelli, S. Miao, D.C. Sinclair, I.M. Reaney, Ti Doping to reduce conductivity in $Bi_{0.85}Nd_{0.15}FeO_3$ ceramics, Adv. Funct. Mater. 21 (2011) 3737.
[9] D. Kan, L. Palova, V. Anbusathaiah, C.J. Cheng, S. Fujino, V. Nagarajan, K.M. Rabe, I. Takeuchi, Universal behaviour and electric-field-induced structural transition in rare-earth-substitued $BiFeO_3$, Adv. Funct. Mater. 20 (7) (2010) 1108–1115.
[10] I.O. Troyanchuk, D.V. Karpinsky, M.V. Bushinsky, O.S. Mantytskaya, N.V. Tereshko, V.N. Shut, Phase transitions, magnetic and piezoelectric properties of rare-earth-substituted $BiFeO_3$ ceramics, J. Am. Ceram. Soc. 94 (12) (2011) 4502–4506.
[11] I. Levin, M.G. Tucker, H. Wu, V. Provenzano, C.L. Dennis, S. Karimi, T. Comyn, T. Stevenson, R.I. Smith, I.M. Reaney, Displacive phase transitions and magnetic structures in Nd-substituted $BiFeO_3$, Chem. Mater. 23 (8) (2011) 2166–2217.
[12] K. Kalantari, I. Sterianou, D.C. Sinclair, P.A. Bingham, J. Pokorný, I.M. Reaney, Structural phase transitions in Ti-doped $Bi_{1-x}Nd_xFeO_3$ ceramics, J. Appl. Phys. 111 (2012) 064107.